

Electrochemical Impedance Spectroscopy and Finite Element Analysis Modeling of a 4-Electrode Humidity Sensor for Natural Gas Transportation Pipelines

Derek M. Hall^a, Timothy Duffy^{a,d}, Margaret Ziomek-Moroz^{b,*} and Serguei N. Lvov^{a,c,d,*}

^aThe EMS Energy Institute, The Pennsylvania State University,
University Park, PA 16802, USA

^bNational Energy Technology Laboratory, U.S. Department of Energy,
Albany, OR 097321 USA

^cDepartment of Materials Science and Engineering, The Pennsylvania State University,
University Park, PA 16802, USA

^dDepartment of Energy and Mineral Engineering, The Pennsylvania State University,
University Park, PA 16802, USA

*Corresponding authors: lvov@psu.edu; Margaret.Ziomek-Moroz@NETL.DOE.GOV

Abstract

Reliable corrosion monitoring of natural gas transmission lines is a major tool providing a foundation for safe management of natural gas infrastructures. Through the development of membrane-based electrochemical sensors able to function in low-conductivity gas environments, corrosion monitoring practices can be further strengthened by real-time monitoring of key risk factors such as relative humidity and corrosion rates of corrodible structures. In this work, we demonstrate and validate how a 4-electrode conductivity sensor can provide a means to monitor relative humidity in gases via electrochemical impedance spectroscopy through finite element analysis (FEA). For a relative humidity range of 5 to 55 %, the impedance response varied from 1 k Ω to 66 k Ω , showing a high sensitivity for gas humidity. To confirm that the measured impedance values reliably interpreted relative humidity, it was found that precise estimation of the sensor's cell constant was needed. FEA was used to assess how the cell constant depended on electrode geometry, membrane geometry and electrode placement within the sensor. Through this approach, assumptions about the characteristic area and length were validated using electrolyte equipotential and current density vector mapping. This reduced possible cell constant uncertainties by 70 %. With a cell constant of 14.84 cm⁻¹, obtained via FEA, membrane conductivity values were in good agreement with published data.

1.0 Introduction

Electrochemical sensors offer a wide range of options for corrosion, corrosion protection and water quality monitoring [1]–[6]. However, conductivity limitations have limited their use in natural gas transmissions lines. Though condensed water sometimes forms, the pipelines are ideally filled with low humidity gases. The Code of Federal Regulations (49 CFR § 192.477) requires natural gas transportation companies to implement an internal corrosion monitoring program for their pipeline corrosion mitigation strategies [7]. Often, these monitoring programs involve: (i) quick field testing of liquid and gas sampling from pipeline drips, where field personnel training and communication have a large impact on the usefulness of the results, (ii) coupon inspection, which normally occurs every 4 to 7 months, (iii) pig programs, which extensively clean and analyze the entire pipe, but are expensive for large pipe networks and cause operational downtime, and less frequently (iv) real-time monitoring systems, such as electrical resistance (ER) probes and linear polarization resistance (LPR) probes. However, the bulk of corrosion processes inside a gas pipeline are only propagated by the presence of

condensed water [8]. Monitoring the local water vapor content and temperature is an attractive real-time monitoring option that could provide reliable insights into the risk of corrosion for a given pipe region. For this reason, an inexpensive electrochemical humidity sensor that can withstand the chemistry, pressures and temperatures observed in many high risk areas should be developed [9]. By probing the conductivity of a humidity-sensitive ion-exchange membrane, using electrochemical impedance spectroscopy, it could be possible to determine the relative humidity of the gas being transmitted and identify the occurrence of water condensation in real-time.

Though many humidity detection methods exist, electrochemical (resistive and capacitive), optical and mass-sensitive types are the most common [10], [11]. Furthermore, the pressures, temperatures and chemical compositions within natural gas transportation systems, especially close to storage wells, exclude the use of most commercial methods to sampling lines at less extreme conditions [11], [12]. As such, the majority of humidity measurements used in the field rely on extrapolation methods to relate humidity data to pipeline conditions. If a sensor could be developed to withstand the harsh conditions found within natural gas transportation systems, then it could significantly improve the understanding of how conditions are evolving in high risk areas of the pipeline.

Recently, electrochemical sensors using ion conductive membranes have been shown to be effective in environments with elevated pressures, temperatures, and CO₂ levels [9]. With further development, this technology may satisfy the current gap in the humidity measurement industry. At its core, this type of humidity sensor would be a 4-electrode electrolyte conductivity probe [13]–[15]. But the effectiveness of an electrochemical sensor is predicated on a reliable connection between conductance measurements and a known dependence between membrane conductivity to water vapor content. This correlation hinges on the calculation of a reliable cell constant (K_{cell}). Though it is common to assume that current travels uniformly through both electrode surfaces and the electrolyte, this assumption can cause large inaccuracies if not validated [14]–[16].

As electrochemical measurements provide only current values and not current density, to describe an intensive property such as conductivity, data collected needs to be corrected by some geometric correction factor. Despite the importance of this normalization process, few studies critically evaluate the validity of the correction factors selected. The consequences of incorrectly assuming these correction factors are most clearly observed in cases where: (1) there are clear differences between electrode and electrolyte geometries and (2) the current distribution across an interface is not uniform. For situations where modeling beyond 1 dimensional space is needed, FEA is a modeling approach that has long been used by many fields of study and is increasing in frequency for the field of electrochemistry [15], [17]–[22]. Here we demonstrate how finite element analysis (FEA) can be used to validate the selection of geometric correction factors and the consequences of using common incorrect assumptions. Furthermore, we provide the approach needed to obtain the cell constant and conductance data needed to use electrochemical conductivity sensors for any sensor geometry.

2.0 Methods

2.1 Sensor Design

Water vapor-dependent ion-conductive membranes were used to provide a way to monitor the water content in natural gas pipelines. The sensor consisted of a 3D-printed electrode holder, an ion-conductive membrane, 4 platinum electrodes, electronic leads, thermocouple, and a steel housing unit. The sensor design and dimensions are given in Figure 1 and Table 1, and the

housing is shown in Figure 2. 3D-printed acrylonitrile butadiene styrene (ABS) polymeric plastic was used as a solid base and hold the 4 electrodes in position relative to the membrane. The use of 3D printed ABS plastic was chosen to keep cost low, the geometry reproducible all while being able to withstand elevated temperatures up to about 90 °C. Though ABS is weakly hydroscopic, ~0.3 % by weight after 350 hours when fully submerged [23], this small uptake did not appear to significantly delay the time required to reach steady state. Likewise, non-hydroscopic and more chemically resistant plastics, such as PTFE, may be more suitable for long-term applications. As-received commercial perfluorinated sulfonic acid ion-exchange Nafion 117 membranes (Chemour, H⁺ form) provided the water-content dependent ion-conductive media for our low-conductivity environment. Nafion 117 was chosen because it has a well-documented history of conductivity dependence with water content [24]–[26]. To maximize the surface area of the membrane exposed to the gas phase while protecting the electrodes, a planar conductivity probe design was implemented.

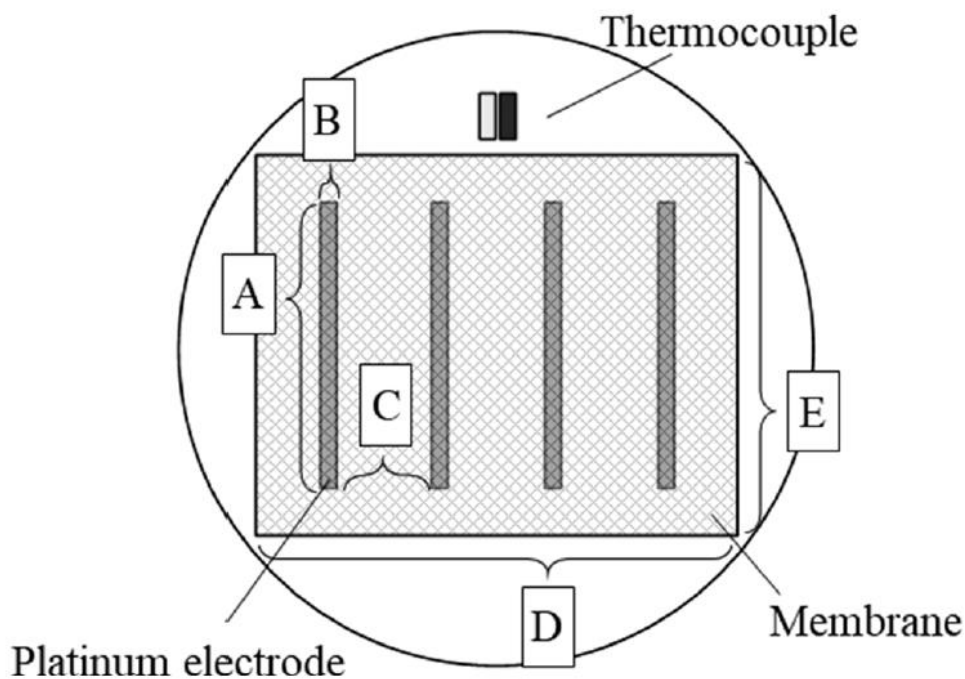


Figure 1. Sensor design.

Table 1. Sensor geometry, with letters indicating the measurements on Figure 1.

Electrodes			
length	A		9.0 mm
diameter	B		0.5 mm
distance	C		3.0 mm
Membrane			
width	D		15.0 mm
height	E		12.0 mm
thickness	-		0.1778 mm

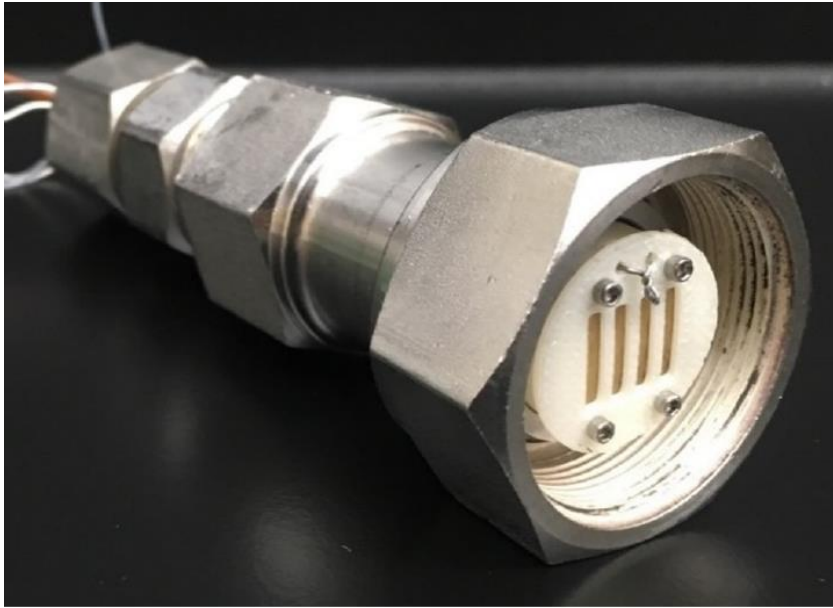


Figure 2. Housing for the sensor. The sensor is shown at the opening on the right, with thermocouple leads and ABS plastic plate to press the membrane to electrode surfaces.

2.2 Flow-through testing system

The setup for these experiments, shown in

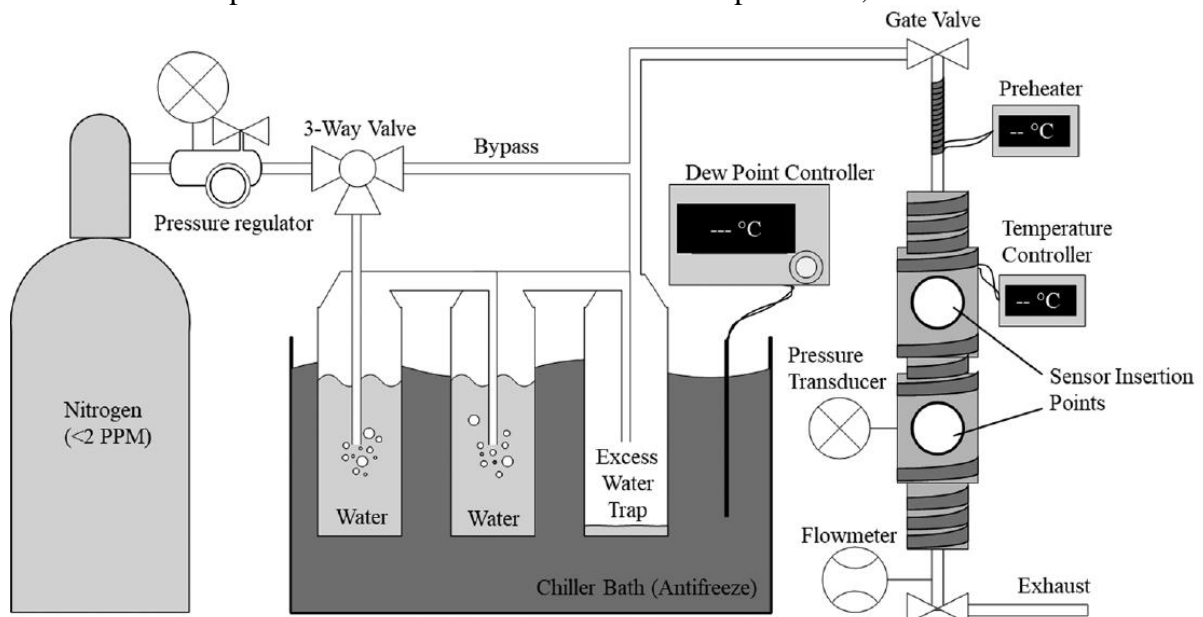


Figure 3, resembles those outlined in ASTM D4178 and D5454 [27], [28]. The test system used commercially available stainless-steel tubing components to flow humidified gas across the sensor surface in a temperature-controlled, pressurized environment. The flow rate and pressure were set to 689 kPa (100 psi) and 3.4 m³/h (2 SCFH), respectively, using pressure valves and a flowmeter. Nitrogen (<2 ppm impurities) from a gas cylinder was bubbled through water vessels submerged in a Polyscience chiller bath to saturate the gas at a specified dew point. The chiller bath temperature was adjusted between 1, 5, 10, 15, and 20 °C to set the dew point of the humidified nitrogen. A commercial humidity sensor (OMEGA HX80) verified the humidity of the gas passing through the system. The gas was then preheated to the desired temperature using 2 OMEGA polyimide film rubber heating tapes around the sensor test system. Each tape was 52 Watts and 0.5 ft by 2 ft. Tests were run moving from dew point 1 to

20 °C for each system temperature, allowing at least 5 hours for the system to reach equilibrium after changing the dew point. The sensors were dried out before each sensor test by flowing dry nitrogen through the testing system. Sensor temperatures of 30, 40, and 60 °C were tested.

2.3 Water content calculation

While there are many ways to report water content in a gas stream, the U.S. natural gas industry represents it as pounds of water per million standard cubic feet of gas (lb/MMscf), where the gas is assumed to be 15.6 °C (60.1 °F) and 0.1 MPa (14.5 psi). Dew point, temperature, pressure, and relative humidity and water content can all be correlated using the tables from ASTM D1142 [29]. The water content of a gas stream is given by Equation 1:

$$W = (C_A/P) + C_B, \quad (1)$$

where W is the water content of the stream (lb/MMscf), P is the total gas pressure (psia), and C_A and C_B are tabulated constants dependent on water-vapor pressure, temperature, and gas composition shown in Table 2 of Ref [29] for values of C_A and C_B . In metric units, 16.02 mg m⁻³ is equivalent to 1 lb/MMscf and will be used for reporting water content here. The water content was experimentally set by saturating the nitrogen at a specified dew point. The quotient between the water content, W , set during the dew-point control and the water content for a saturated gas stream at the experimental temperature, $W_{T,Sat}$, gives the relative humidity according to Equation 2:

$$RH(\%) = W/W_{T,Sat} \quad (2)$$

For natural gas pipeline operators, a general rule of thumb is to keep pipeline water content below 112 mg m⁻³ (7 lb/MMscf) for internal corrosion mitigation programs [9].

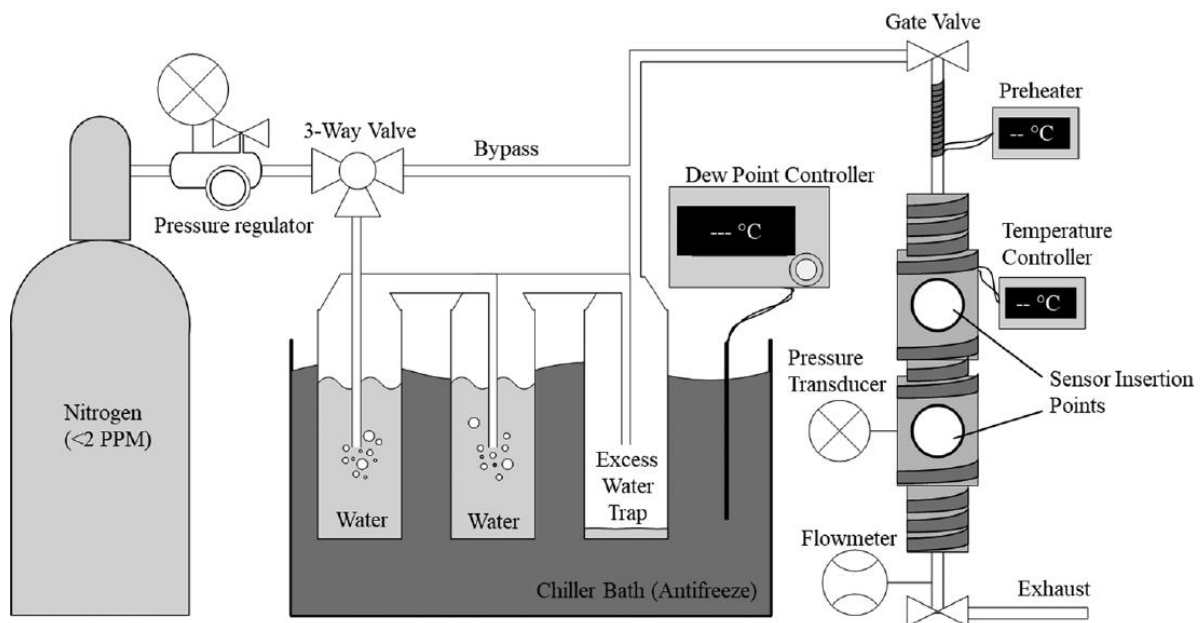


Figure 3. Schematic of the flow-through testing system as described in Section 2.2.

2.4 Resistance Measurements

A Gamry PCI4 750 potentiostat measured the complex impedance across the membrane using the four-electrode, potentiostatic electrochemical impedance spectroscopy (EIS) technique. The potential between the two inner platinum electrodes was alternated between ± 20 mV from

the open circuit potential across a frequency range of 10 to 1500 Hz. This range was selected because it routinely captured the lowest phase angles that were representative of a purely resistive impedance. The current between the outer electrodes was monitored. The complex impedance was obtained from these potential-current pairs and the delay between the current's response times. All complex impedances across the entire frequency range showed a phase angle of less than 4°, implying that experimental artefacts were adequately reduced. The impedance data were interpolated to 0° phase angle to calculate the resistance, R , of the membrane.

2.5 Cell Constant Models

Conductivity, κ , is commonly determined via a well-known relation between the measured R values and the cell constant (K_{cell}) [30]. For reliable interpretation of κ values, the K_{cell} for the sensor must be clearly defined. Equation 3 relates κ (S cm^{-1}) to K_{cell} (cm^{-1}) and R (Ω):

$$R = A/(l\kappa) = K_{\text{cell}}/(\kappa), \quad (3)$$

where A is the characteristic cross-sectional area (usually in cm^2) and l is the characteristic length of the current path (in cm). As the geometry of this planar sensor varies in 3 dimensions, appropriate length and area values are not immediately clear. Therefore, the following questions arise: Would the area of the electrode or that of the membrane be more appropriate in Equation 3? Likewise, what characteristic length typifies a 4-electrode measurement?

For reliable interpretation of a cell constant, the FEA software COMSOL with its electrochemical module was employed. This approach allowed us to determine the current path taken using Ohm's law and charge balance constraints for multiple elements over 3D space. To achieve this, a primary current distribution model was used to quantify the potential field generated throughout the membrane in response to ionic current conduction [31]. Through this approach, we were able to determine the cell constant for a given electrode/membrane configuration, despite complex current pathways.

Using the primary current model, a potential difference resulting from a constant conductivity domain, in this case the membrane, was determined using the boundary condition of a constant current passing between the two outer electrodes. The top (outer) electrode surface was given a constant-current boundary condition of 1 μA ; the boundary condition for the bottom (outer) electrode surface was a grounded electric potential. These boundary conditions generated the electrolyte potential distribution across the membrane domain. For this simulation, the conductivity of the membrane was fixed to 0.16 S m^{-1} . The inner electrodes had discrete potential values across their surfaces, each dependent on their surrounding electrolyte potentials. These discrete values were simulated by linking the two inner electrodes with an external resistance of $10^{14} \Omega$ akin to an open circuit potential measurement using a high impedance electrometer. The membrane domain was filled with 79654 tetrahedral elements that were generated using the finer mesh software option. Extra fine and extremely fine meshes were tested, but model results did not change by more than 0.2 %. The element volume ratio for the finer mesh option was 0.001043.

As a comparison, two conventional cell constants were calculated using Equation 3. The first K_{cell} (referred to as A1) assumes (i) the cell constant length is the distance between the inner edges of the inner electrodes (0.3 mm) and (ii) the area is the product of the membrane thickness (0.1778 mm) and the membrane height (12 mm). This results in a K_{cell} value of $A1 = 14.06 \text{ cm}^{-1}$. A1 represents the smallest K_{cell} possible given the sensor components. The second (A2)

assumes (i) the length was best represented by the outer edges of the inner electrodes (0.4 mm) and (ii) the area was the product of the membrane thickness and the electrode height (9 mm). These assumptions resulted in a value of $A_2 = 25 \text{ cm}^{-1}$ which was about 70 % larger than A_1 .

3.0 Results and Discussion

3.1 Electrochemical Impedance Spectroscopy

As exemplified in Figure 4, the 4-electrode EIS impedance data were simple to interpret. The phase angles were all close to 0° and the magnitude of the measured impedance (Z_{mag}) showed a stable value across the frequency range 10 to 150 Hz. The sensors demonstrated negligible experimental artefact for all conditions tested.

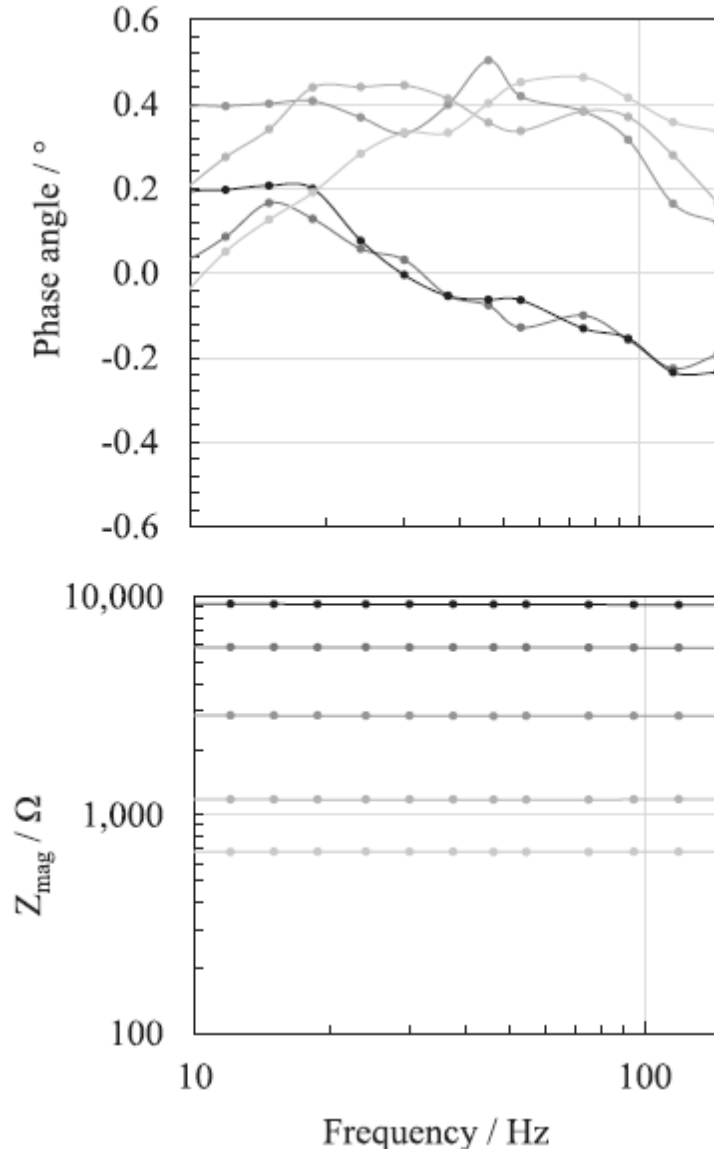


Figure 4. Phase angle (top) and impedance (bottom) data for EIS tests at 30 °C. The different shaded points correspond to the different dew-points: “●” 1 °C, “●” 5 °C, “●” 10 °C, “●” 15 °C, and “●” 20 °C.

Extracting the impedance data to a phase angle of 0° , the resistance of the Nafion 117 membrane across the conditions tested is shown in Figure 5 and Figure 6. As expected, the obtained resistance values decreased as water content increased and temperature decreased. All quantities are given in

the Appendix. Resistance values showed a nonlinear dependence on water content and temperature.

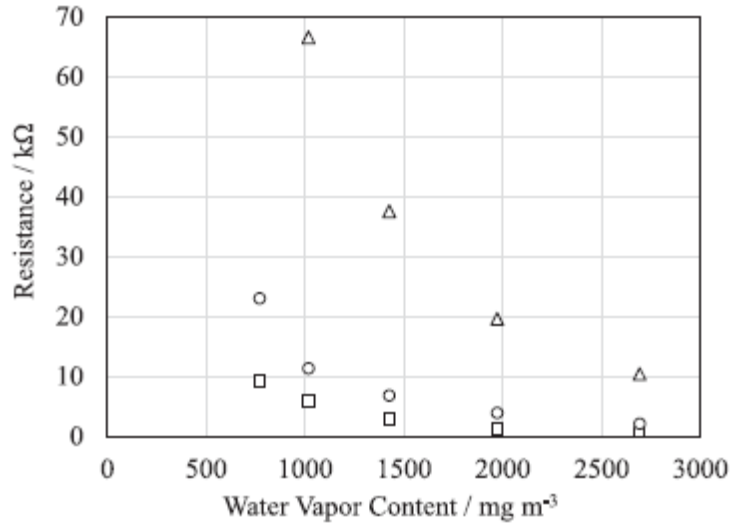


Figure 5. Membrane resistance versus water content for the sensor shown in Figure 1. Points correspond to temperatures of “□” 30 °C, “○” 40 °C, and “Δ” 60 °C, all tested at 689 kPa and a flow rate of 3.4 m³/h.

Figure 6 shows that the resistance varied non-linearly with relative humidity, and that the temperature effect was less pronounced if relative humidity was held constant.

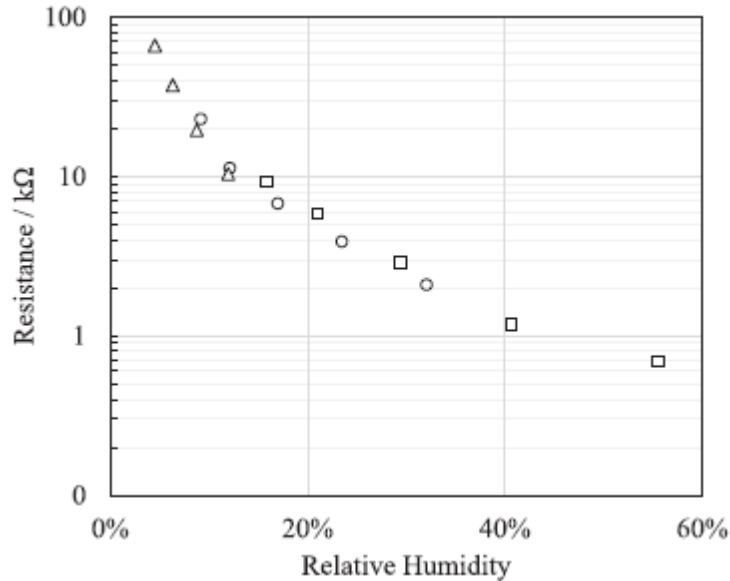


Figure 6. Resistance across membrane for all data points vs. the experimental relative humidity. Points correspond to temperatures of “□” 30 °C, “○” 40 °C, and “Δ” 60 °C, all tested at 689 kPa and a flow rate of 3.4 m³/h.

The response from three sensors were all found to provide resistance responses within 5 % of each other for 5 different dew points, indicating good repeatability.

3.2 FEA Modeling Results

The primary current distribution model results affirmed the importance of understanding the how the surface area of each electrode, electrode placement and electrolyte dimensions all contribute to the cell constant. Figure 7 shows how non-uniformity of the potential field within the membrane develops then dissipates after about 1 mm from each of the outer electrodes. Some non-uniformity was also induced by the inner electrodes, but this appears to be minimal in this case when compared to the influence of the outer electrodes. Furthermore, the current density vector arrows show that current paths expand to fill the entire membrane domain between the two outer electrodes. Figure 7 presents the electrolyte current density vectors and equipotential lines modeled for the membrane using the values listed in cell constant modeling Section 2.5.

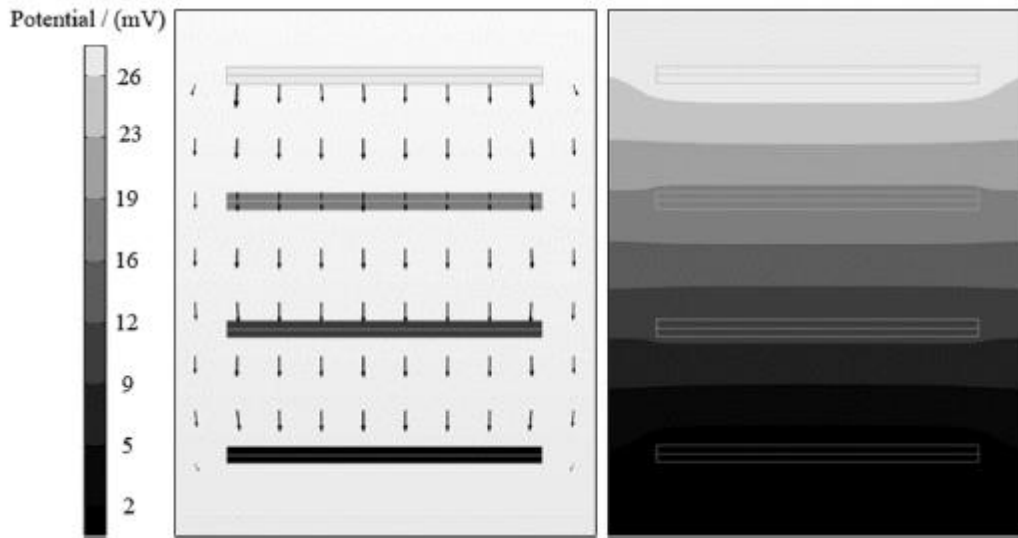


Figure 7. Electrolyte current density vector map (left) and equipotential map (right) across the sensor membrane, corresponding to dimensions in Table 1. Result corresponds to 1 μA of simulated current across a membrane with $\kappa = 1.6 \times 10^{-3} \text{ S cm}^{-1}$.

The impact of the inner electrodes is best seen by comparing the electric potentials of the inner electrodes to the electrolyte equipotential lines around the inner electrodes. FEA modeling indicated that the potential difference between the inner electrodes was 9.277 mV, using electric potential values of 18.768 mV and 9.491 mV found at the inner electrode surfaces. This potential difference divided by the 1 μA input current gave a resistance value of 9280 Ω . This calculated resistance value was then divided by the input conductivity value to provide a cell constant of 14.84 cm^{-1} . This cell constant was found to be independent of the membrane's conductivity. The constant-current boundary condition, and membrane conductivity values had no impact on the final cell constant calculation. This is due the reliance of the primary current model on Ohm's law. Any change in the input current or conductivity simply changes the output potential in a manner dictated by the cell constant which is only a function of the geometry. As such, the calculated cell constant only depends on the geometry of the electrodes, their placement and the membrane geometry. A closer inspection of the current density distribution across the inner electrode surfaces revealed that essentially all the current was passing through the inner edges of these electrodes. This current density localization explains why the inner electrode potentials matched electrolyte potentials found at the inner electrode's inside edges as opposed to electrolyte potentials at their

center or outer edges. As such, the length value that best matched the FEA modeled cell constant was closest to the length between the inner edges of the inner electrodes (0.3 mm).

As can be seen from Figure 8, the final conductivity values were significantly impacted by varying the assumptions of area and length. Figure 8 compares the FEA-determined cell constant to the two cell constants calculated using equation 3.

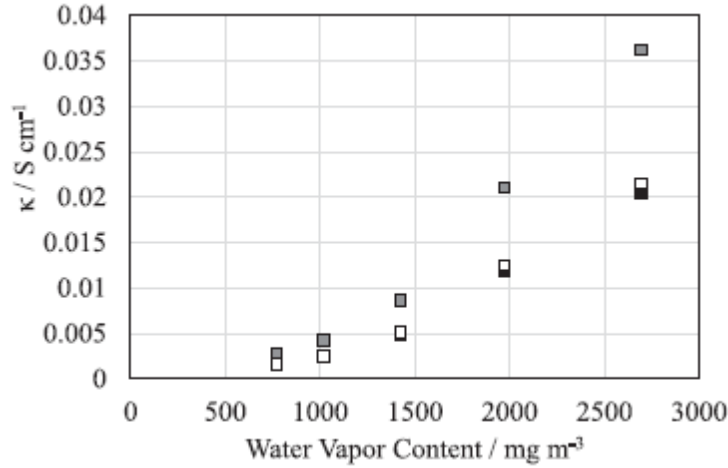


Figure 8. Conductivity values for 30 °C as a function of water vapor content when $K_{\text{cell}} = 25 \text{ cm}^{-1}$ (■), 14.06 cm^{-1} (■) and the FEA-calculated 14.84 cm^{-1} (□).

3.3 Humidity Sensor Conductivity

For natural gas pipeline monitoring, we would like to predict the local water content from conductivity tests using a simple correlation. If a thermocouple is incorporated onto the sensor, or the temperature of the gas stream is known at the monitoring location, both the relative humidity and water content can be calculated. For the experimental data in this study, Equation 4.a resembling the correlation used in [26] was fit to the data of the current study:

$$RH = \kappa^{1/2} D e^{E_A/2RT} \quad (4.a)$$

Where RH is in %, κ is in units of S cm^{-1} , D is an empirical constant ($0.46 \text{ cm}^{1/2} \text{ S}^{-1/2}$) T is in units of K , E_A is the activation energy for proton transport (fitted to 10731 J mol^{-1} , compared to 10440 J mol^{-1} from [26]) and R is the gas constant ($8.314 \text{ J K}^{-1} \text{ mol}^{-1}$.) We've assumed an Arrhenius temperature correlation, a power relationship with relative humidity, and we've assumed that the activation energy E_A of proton transport is independent of temperature and humidity. The water vapor content (mg m^{-3}) can be further calculated using Equation 4.b and the data tables from ASTM D1142 [29].

$$W = W_{\text{sat}} \times \kappa^{1/2} D e^{E_A/2RT} \quad (4.b)$$

A comparison of these equations with experimental data is shown in Figure 9. Equation (4.b) has an R^2 coefficient greater than 99 % when compared with the experimental data, implying an excellent goodness-of-fit.

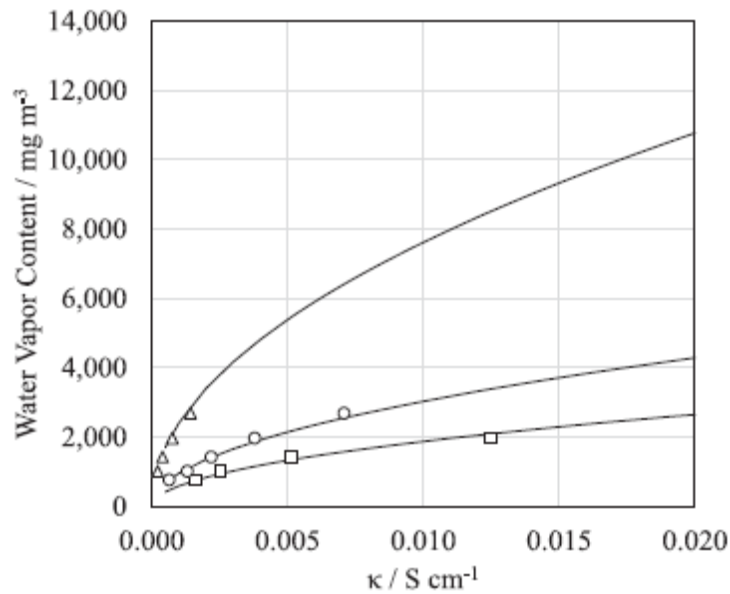


Figure 9. Comparison of Equation (4.b) with experimental results. Points correspond to temperatures of “□” 30 °C, “○” 40 °C, and “Δ” 60 °C, all tested at 689 kPa and a flow rate of 3.4 m³/h.

The experimental data, after interpretation of the K_{cell} , have good agreement with the existing literature. Data for conductivity of the Nafion 117 membrane at 30 °C with varying humidity is shown in Figure 10.

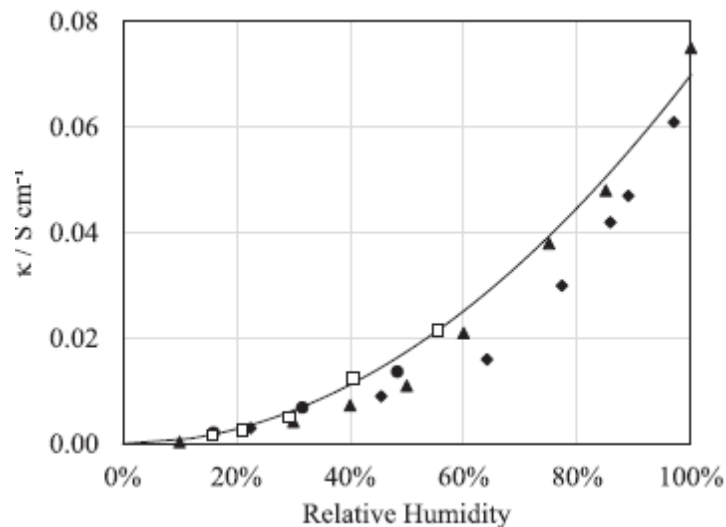


Figure 10. Comparison of conductivity-humidity data between literature values at 30 °C. The solid line is equation (4), the data are from “□” this work, “●” Beck et al. [9], “▲” Yadav and Fedkiw [26], and “◆” Zadawinski et al. [32],

After using FEA to determine a representative cell constant for the humidity sensor, the data followed the expected trends published in literature. However, many of the published data sources

for membrane conductivity have little to no explanation of their cell constants. As such, some of the variation observed in Figure 10 could be attributed to assumed cell constants.

4.0 Conclusions

A reproducible 4-electrode membrane-based conductivity sensor was developed for use in natural gas transmission environments. This sensor provides a means to monitor water vapor content in key areas susceptible to corrosion from condensed water. Electrochemical impedance spectroscopy data was used to determine the resistance of the probe a function of temperature and water vapor content in a laboratory environment. After plotting membrane conductivity as a function of relative humidity, the additional impact of temperature was far less significant over the temperature range studied. Overall, good agreement was found between the data obtained in this study and previous studies of Nafion 117. As such, the dimensions selected for the electrodes and membrane provided a sufficiently large cell constant that provided measurable impedances for the range of conductivities observed from Nafion 117 in the environments of interest.

A key component to interpreting water vapor content from the data collected was the determination of a reliable cell constant. Finite element analysis provided a means to evaluate how sensor design choices affected the current path. Using this approach, it was possible to assess how membrane and electrode geometries contributed to the current-potential data collected from the conductivity sensor. The electrode positioning used in this study provided enough space for the current path to extend into the membrane area available between the current electrodes. As such, our primary current distribution model results indicated that the cell constant was significantly closer to the A1 cell constant assumptions, i.e. a short length and large area. Through this study, we found that FEA is a powerful tool for assessing how choices of sensor geometry impacted utilization of the active materials and the resulting cell constant. Likewise, FEA provides a method to model how the impedance of an electrochemical sensor system can be adjusted to satisfy size limitations, material costs and equipment constraints.

5.0 Acknowledgements and Disclaimer

This work was completed as a part of National Energy Technology Laboratory's (NETL) research for the Department of Energy's Natural Gas Infrastructure Program. As such, this article was prepared as an account of work sponsored by an agency of the United States Government. Neither the United States Government nor any agency thereof, nor any of their employees, makes any warranty, express or implied, or assumes any legal liability or responsibility for the accuracy, completeness, or usefulness of any information, apparatus, product, or process disclosed, or represents that its use would not infringe privately owned rights. Reference herein to any specific commercial product, process, or service by trade name, trademark, manufacturer, or otherwise does not necessarily constitute or imply its endorsement, recommendation, or favoring by the United States Government or any agency thereof. The views and opinions of authors expressed herein do not necessarily state or reflect those of the United States Government or any agency thereof.

6.0 Appendix: Data Collected

Temperature/°C	Dew-Point /°C	Water content /mg m ⁻³	RH/%	Resistance /kΩ
30	1.0	769	16	9.2
	5.0	1017	21	5.9
	10.0	1426	29	2.9
	15.0	1972	41	1.2
	20.0	2693	55	0.7
40	1.0	769	9	23.0
	5.0	1017	12	11.3
	10.0	1426	17	6.8
	15.0	1972	23	3.9
	20.0	2693	32	2.1
60	5.0	769	5	66.6
	10.0	1017	6	37.5
	15.0	1426	9	19.6
	20.0	1972	12	10.4

7.0 References

- [1] D. M. Hall, J. R. Beck, E. Brand, M. Ziomek-Moroz, and S. N. Lvov, "Copper-Copper Sulfate Reference Electrode for Operating in High Temperature and High Pressure Aqueous Environments," *Electrochim. Acta*, vol. 221, pp. 96–106, 2016.
- [2] D. M. Hall, J. Beck, S. Lvov, and M. Ziomek-Moroz, *Review of pH and reference electrodes for monitoring corrosion in HPHT extreme environments*, vol. 2015–Janua. 2015.
- [3] S. N. Lvov, "Electrochemical Techniques for Studying High Temperature Subcritical and Supercritical Aqueous Systems," in *Encyclopedia of Electrochemistry*, A. Bard, M. Stratmann, D. D. Macdonald, and P. Schmuki, Eds. Wiley-VCH, 2007, pp. 723–747.
- [4] S. N. Lvov, X. Y. Zhou, S. M. Ulyanov, and a. V. Bandura, "Reference systems for assessing viability and accuracy of pH sensors in high temperature subcritical and supercritical aqueous solutions," *Chem. Geol.*, vol. 167, no. 1–2, pp. 105–115, Jun. 2000.
- [5] B. Raman, D. M. Hall, S. J. Shulder, M. F. Caravaggio, and S. N. Lvov, "An experimental study of deposition of suspended magnetite in high temperature-high pressure boiler type environments," *Colloids Surfaces A Physicochem. Eng. Asp.*, vol. 508, pp. 48–56, 2016.
- [6] R. Feng, J. Beck, M. Ziomek-Moroz, and S. N. Lvov, "High-Temperature Electrochemical Corrosion of Ultra-High Strength Carbon Steel in H₂S-Containing Alkaline Brines," *Electrochim. Acta*, vol. 241, pp. 341–352, 2017.
- [7] Department of Transportation, "49 CFR 192.477 - Internal corrosion control: Monitoring."

- 2017.
- [8] NACE International, “SP 0106-06 Control of Internal Corrosion in Steel Pipelines,” no. 21111, 2006.
 - [9] J. Beck, D. M. Hall, M. Ziomek-Moroz, and S. N. Lvov, “Membrane-coated electrochemical sensor for corrosion monitoring in natural gas pipelines,” *Sensors & Transducers*, vol. 77, no. 11, pp. 28–33, 2017.
 - [10] T. A. Blank, L. P. Eksperiandova, and K. N. Belikov, “Recent trends of ceramic humidity sensors development: A review,” *Sensors Actuators, B Chem.*, vol. 228, pp. 416–442, 2016.
 - [11] J. G. Gallegos *et al.*, “An investigation of the comparative performance of diverse humidity sensing techniques in natural gas,” *J. Nat. Gas Sci. Eng.*, vol. 23, pp. 407–416, 2015.
 - [12] J. G. Gallegos, S. Avila, R. Benyon, G. McKeogh, and A. Stokes, “Experimental evaluation of the performance of humidity analyzers in natural gas under industrial conditions,” *J. Nat. Gas Sci. Eng.*, vol. 31, pp. 293–304, 2016.
 - [13] F. P. Anderson, H. C. Brookes, M. C. B. Hotz, and A. H. Spong, “Measurement of electrolyte conductance with a four-electrode alternating current potentiometer,” *J. Phys. E.*, vol. 2, no. 6, pp. 499–502, 1969.
 - [14] Z. Xie *et al.*, “Discrepancies in the Measurement of Ionic Conductivity of PEMs Using Two- and Four-Probe AC Impedance Spectroscopy,” *J. Electrochem. Soc.*, vol. 153, no. 10, p. E173, 2006.
 - [15] T. Grysiński and Z. Moroń, “Planar sensors for local conductivity measurements in biological objects - Design, modelling, sensitivity maps,” *Sensors Actuators, B Chem.*, vol. 158, no. 1, pp. 190–198, 2011.
 - [16] E. J. Zimney, G. H. B. Dommett, R. S. Ruoff, and D. A. Dikin, “Correction factors for 4-probe electrical measurements with finite size electrodes and material anisotropy: A finite element study,” *Meas. Sci. Technol.*, vol. 18, no. 7, pp. 2067–2073, 2007.
 - [17] X. Duan, W. Jiang, Y. Zou, W. Lei, and Z. Ma, “A coupled electrochemical–thermal–mechanical model for spiral-wound Li-ion batteries,” *J. Mater. Sci.*, vol. 53, no. 15, pp. 10987–11001, 2018.
 - [18] E. J. F. Dickinson, H. Ekström, and E. Fontes, “COMSOL Multiphysics®: Finite element software for electrochemical analysis. A mini-review,” *Electrochem. commun.*, vol. 40, pp. 71–74, 2014.
 - [19] I. J. Cutress, E. J. F. Dickinson, and R. G. Compton, “Analysis of commercial general engineering finite element software in electrochemical simulations,” *J. Electroanal. Chem.*, vol. 638, no. 1, pp. 76–83, 2010.
 - [20] M. A. Khaleel, Z. Lin, P. Singh, W. Surdoval, and D. Collin, “A finite element analysis modeling tool for solid oxide fuel cell development: Coupled electrochemistry, thermal and flow analysis in MARC®,” *J. Power Sources*, vol. 130, no. 1–2, pp. 136–148, 2004.
 - [21] H. Lavelaine de Maubeuge, “Calculation of the Optimal Geometry of Electrochemical Cells,” *J. Electrochem. Soc.*, vol. 149, no. 8, p. C413, 2002.
 - [22] N. S. Vasile, A. H. A. Monteverde Videla, and S. Specchia, “Effects of the current density distribution on a single-cell DMFC by tuning the anode catalyst in layers of gradual loadings: Modelling and experimental approach,” *Chem. Eng. J.*, vol. 322, pp. 722–741, 2017.
 - [23] M. Sefa, Z. Ahmed, J. A. Fedchak, J. Scherschligt, and N. Klimov, “Gas uptake of 3D

- printed acrylonitrile butadiene styrene using a vacuum apparatus designed for absorption and desorption studies,” *J. Vac. Sci. Technol. A Vacuum, Surfaces, Film.*, vol. 34, no. 6, p. 061603, 2016.
- [24] S. Ma, Z. Siroma, and H. Tanaka, “Anisotropic Conductivity Over In-Plane and Thickness Directions in Nafion-117,” *J. Electrochem. Soc.*, vol. 153, no. 12, p. A2274, 2006.
- [25] Y. Sone, “Proton Conductivity of Nafion 117 as Measured by a Four-Electrode AC Impedance Method,” *J. Electrochem. Soc.*, vol. 143, no. 4, p. 1254, 1996.
- [26] R. Yadav and P. S. Fedkiw, “Analysis of EIS Technique and Nafion 117 Conductivity as a Function of Temperature and Relative Humidity,” *J. Electrochem. Soc.*, vol. 159, no. 3, pp. B340–B346, 2012.
- [27] ASTM International, “ASTM D4178-99,” 1999.
- [28] ASTM International, “ASTM D5454-11,” 2011.
- [29] ASTM International, “ASTM D1142-95,” 2000.
- [30] S. N. Lvov, *Introduction to Electrochemical Science and Engineering*, 1st ed. Boca Raton, FL: CRC press Inc, 2015.
- [31] K. T.-A. John Newman, *Electrochemical Systems*, 3rd ed. 2004.
- [32] T. A. Zawodzinski *et al.*, “A Comparative Study of Water Uptake By and Transport Through Ionomeric Fuel Cell Membranes,” *J. Electrochem. Soc.*, vol. 140, no. 7, pp. 1981–1985, 1993.